

Application of silver-exchanged zeolite for radioxenon mitigation at fission-based medical isotope production facilities

Peer-reviewed author version

GUEIBE, Christophe; Rutten, Jos; CAMPS, Johan; Moyaux, Dominique; SCHROEYERS, Wouter; Auer, Matthias & SCHREURS, Sonja (2022) Application of silver-exchanged zeolite for radioxenon mitigation at fission-based medical isotope production facilities. In: Process safety and environmental protection, 158 , p. 576 -588.

DOI: 10.1016/j.psep.2021.12.031

Handle: <http://hdl.handle.net/1942/36504>

Title: Application of silver-exchanged zeolite for radioxenon mitigation at fission-based medical isotope production facilities

Authors: Christophe Gueibe<sup>a,b</sup>, Jos Rutten<sup>a</sup>, Johan Camps<sup>a,b</sup>, Dominique Moyaux<sup>c</sup>, Wouter Schroeyers<sup>b</sup>, Matthias Auer<sup>d,1</sup>, Sonja Schreurs<sup>b</sup>

<sup>a</sup> Belgian Nuclear Research Centre (SCK CEN), Boeretang 200, 2400 Mol, Belgium

<sup>b</sup> Hasselt University (UHasselt), CMK, NuTeC, Nuclear Technology – Faculty of Engineering Technology, Agoralaan Building H, 3590 Diepenbeek, Belgium

<sup>c</sup> Institute for RadioElements (IRE), Avenue de l'Espérance 1, 6220 Fleurus, Belgium

<sup>d</sup> Comprehensive Nuclear Test-Ban Treaty Organization (CTBTO), Vienna International Centre, PO Box 1200, 1400 Vienna, Austria

Corresponding author:

E-mail: christophe.gueibe@sckcen.be

Postal address: Belgian Nuclear Research Centre (SCK CEN), Boeretang 200, 2400 Mol, Belgium

---

<sup>1</sup> Present address: Instrumental Software Technologies, Inc., 77 Van Dam Street, Suite 9, Saratoga Springs, NY 12866, USA

Title: Application of silver-exchanged zeolite for radioxenon mitigation at fission-based medical isotope production facilities

## Abstract

Atmospheric radioxenon releases from fission-based medical isotope production facilities are the main contributors to the radioxenon background being observed in the International Monitoring System (IMS) for the verification of the Comprehensive Nuclear-Test-Ban Treaty. This background is impacting the detection capability of the IMS network for potential nuclear explosions. Reducing the radioxenon emissions from these facilities requires the optimization of the corresponding filtration process. The investigation of more efficient Xe adsorption materials than Activated Carbon (AC), which is currently used for this application, can play an important role for such an optimization. In this work, the Xe adsorption capacity of silver-exchanged zeolites (AgZs) is compared to the one of ACs in relevant conditions for fission-based medical isotope production facilities. The most promising AgZ candidate, a silver-exchanged titanasilicate (Ag-ETS-10), is investigated in more detail for its application to further reduce radioxenon releases. As operational conditions depend on the production and off-gas treatment processes, the effect of Xe concentration, flow rate, temperature and moisture on the Xe adsorption in Ag-ETS-10 is reported. Furthermore, since AgZs are far more expensive than ACs, it is crucial to be able to regenerate the material, whilst maintaining its full Xe adsorption properties for successive reuse. Accordingly, the durability of Ag-ETS-10 is investigated with regard to desorption and adsorption cycles but also with regard to gamma irradiation.

Keywords: Xenon adsorption, Regeneration, Silver-exchanged zeolite, Activated carbon, CTBT verification, Medical isotope production facilities

## 1. Introduction

During the past two decades, the Comprehensive Nuclear-Test Ban Treaty Organization (CTBTO) has been deploying a network, the International Monitoring System (IMS), with four types of monitoring technologies (seismic, infrasound, hydroacoustic and radionuclide), around the globe, designed to detect possible violations of the CTBT (Comprehensive Nuclear-Test-Ban Treaty, 1996). Among all these monitoring sensors, half of the eighty radionuclide sensors are foreseen to contain Noble Gas (NG) monitoring systems. Currently 31 of the planned 40 systems have been installed (CTBTO, 2021). The NG monitoring systems are designed to measure four radioxenon isotopes of relevance for CTBT monitoring: Xe-131m, Xe-133m, Xe-133 and Xe-135, with half-lives of 11.9 days, 2.19 days, 5.24 days and 9.14 h, respectively. These Xe isotopes are particularly relevant for CTBT verification due to their inert nature, fission yield, and half-life.

It became clear in the previous two decades that a worldwide radioxenon background, coming from civilian sources, is being observed in the NG monitoring systems (Achim et al., 2021; Auer et al., 2004; Hoffman et al., 2009; Saey et al., 2010b; Saey et al., 2006). The researchers in this field have collected a large amount of data on the inventory of radioxenon released to the atmosphere by different civilian nuclear installations and their potential impact on the IMS (Achim et al., 2016; Gueibe et al., 2017; Kalinowski and Tatlisu, 2020; Saey, 2009; Wotawa et al., 2010; Zahringer et al., 2009). This radioxenon release information is being refined by the use of high resolution stack monitoring at some installations (Goodwin et al., 2021; Ringbom et al., 2020). The main sources of radioxenon releases to the atmosphere were determined to be a limited

number of fission-based Medical Isotope Production Facilities (MIPFs) around the globe. Nuclear Power Plants (NPPs) can also contribute to some of the radioxenon observations particularly for NG monitoring systems nearby NPPs (De Meutter et al., 2016; Ringbom et al., 2020). Even though these radioxenon releases are well below national regulations for the protection of the public and environment, they are still high enough to be detected by the very sensitive IMS NG systems (Doll et al., 2014).

The current knowledge on civilian radioxenon releases is not sufficient to understand all observations in the IMS NG network, which would be required to be able to confidently discriminate between possible detections from a nuclear explosion and the normal background observations (Bowyer, 2020; Goodwin et al., 2020). When multiple Xe isotopes are observed, Xe isotopic ratios can be used to discriminate between civilian sources and nuclear tests (Kalinowski et al., 2010). However, as shown by the likely radioxenon detections from four of the six nuclear tests performed by the Democratic People's Republic of Korea (De Meutter et al., 2017; Gaebler et al., 2019; Ringbom et al., 2014; Saey et al., 2007), the samples were containing only one or two Xe isotopes which is not sufficient for isotopic discrimination. Furthermore, the continuous background at some locations can shift the observed isotopic ratio of a potential nuclear explosion away from its expected isotopic signature (Bowyer, 2020). Finally, the fission-based MIPFs have a radioxenon signature that is close to the one that would be expected from a nuclear explosion (Saey et al., 2010a).

In order to minimize the impact of these civilian sources on the IMS NG network, Bowyer et al. (2013) proposed an upper level of 5 GBq/day for radioxenon releases from fission-based MIPFs. The worldwide radioxenon background is expected to become even more complex in the near future due to new emerging fission-based MIPFs (NEA, 2019). It will thus be increasingly critical to reduce the radioxenon releases from these facilities (Bowyer et al., 2014). The Xe-133 releases from the largest fission-based MIPFs are estimated to be on average in a range from 1 to 10 TBq per day (Gueibe et al., 2017), which would thus need an additional decay period of 40 to 57 days to reach the proposed upper level. The fission-based MIPFs are producing radioisotopes, mainly Mo-99 and its daughter product Tc-99m, for medical applications through the dissolution of irradiated uranium targets. The main Xe release, in the ventilation system, is directly the result of the target dissolution, where the off-gases are driven out of the dissolver by an He or N<sub>2</sub> flow for their subsequent treatment (Sameh, 2013). The typical flow rate used is in the order of 1000 cm<sup>3</sup>/min for a duration of about one hour (Faga et al., 2018; Metz et al., 2014; PNNL, 2018).

The current method used for mitigating radioxenon releases in fission-based MIPFs, and in nuclear installations in general, is through the adsorption of Xe on Activated Carbons (AC), possibly with the combination of gas storage tanks, as this is a well-proven technique and is the most convenient method for such applications (Doll et al., 2014; Kepak, 1990; Moeller and Underhill, 1981; Munakata et al., 1999; Underhill, 1981; Zhou et al., 2011). The adsorbed Xe is trapped in AC for a certain period of time to allow sufficient decay before being released to the atmosphere. The Xe adsorption on AC requires either a large volume of AC or a cooling system to operate the AC at low temperatures for an efficient Xe adsorption (Lee et al., 2016). ACs have also the disadvantage of increasing the risk of fire (Doll et al., 2014). Furthermore, there is a preference for passive systems that do not require an active cooling system as this could lead to uncontrolled radioxenon releases in case of failure. Existing facilities have an additional challenge to further decrease their radioxenon emissions as they have limited space/footprint available to implement a more efficient radioxenon mitigation system.

Due to the ignition risk with AC, researchers have been investigating the use of zeolites, as they are non-combustible. Several studies demonstrated that zeolites had a lower Xe adsorption capacity than AC at room temperature (Ianovski et al., 2002; Kitani and Takada, 1965; Munakata et al., 1999). However, it has been demonstrated that silver-exchanged zeolites (AgZs) offer a significantly higher Xe adsorption capacity at room temperature compared to AC at low Xe partial pressures (Byun and Hahm, 2020; Deliere et al., 2016; Monpezat et al., 2019; Munakata et al., 2003). To the best of our knowledge, the application of silver-exchanged zeolites for radionuclide mitigation at fission-based MIPFs has not yet been specifically reported in the literature. More recently, a new class of porous materials, called Metal-Organic Frameworks, have been investigated for Xe/Kr separation and showed promising results for this specific separation (Banerjee et al., 2018). However, these materials have currently a Xe adsorption capacity at room temperature that is in the same range as the one from AC (Banerjee et al., 2018) and would thus currently not improve the efficiency of radionuclide mitigation with regard to the volume and footprint required.

In this work, the authors investigated the use of AgZs for the capture of radionuclide releases from the dissolution process of fission-based MIPFs to provide a potential solution to further reduce the emissions while maintaining the same volume and footprint for the system. First, different AgZs are compared to typical ACs used in the nuclear industry. Based on this comparison, the most promising AgZ, a silver-exchanged titanosilicate zeolite (Ag-ETS-10), is further investigated for its use and durability in this specific context.

## 2. Materials and methods

Two types of Xe adsorbents were selected for this study, namely: ACs (as reference adsorbent) and AgZs (section 2.1). In order to investigate the Xe adsorption properties of the different adsorbents, an experimental system was designed to perform Xe breakthrough measurements (section 2.2) in varying conditions of Xe concentration, flow rate, temperature and moisture content. Finally, the durability of one of the AgZs against gamma irradiation was investigated in a gamma irradiation facility at the Belgian Nuclear Research Centre (section 2.3).

### 2.1. Adsorbents

Three ACs and five AgZs were investigated. Their supplier, type, and commercial name together with their density, mesh size and silver content, as provided by the supplier with the acquired sample, are presented in Table 1.

**Table 1. Overview of the adsorbents studied in this work with their density, mesh size, and, when applicable, silver content.**

Supplier	Type of adsorbent	Material name	Density (g/cm <sup>3</sup> )	Mesh size (mm)	Ag (wt. %)
Cabot Norit Nederland B.V.	AC	Norit RKJ 1	0.52	0.707-4.76	NA
NUCON International Inc.	AC	Nusorb® GXK	0.50	1.68-3.36	NA
Chemviron Carbon	AC	Nuclearcarb® 203C	0.57	1.68-3.36	NA
Sigma Aldrich Co.	AgZ	Ag-Mordenite	1.07	1.68-4.76	10-15
Extraordinary Adsorbents	AgZ	Ag-ETS-10_1	0.90	0.297-0.841	25-30
Extraordinary Adsorbents	AgZ	Ag-ETS-10_2	1.10	0.297-0.841	25-30
Extraordinary Adsorbents	AgZ	Ag-Chabazite_1	0.57	0.297-0.841	10-15
Extraordinary Adsorbents	AgZ	Ag-Chabazite_2	0.63	0.297-0.841	25-30

The selected ACs are commercially available adsorbents especially developed for the capture of radioactive gases in the nuclear industry. Both the Nuclearcarb® 203C and Nusorb® GXK samples are coconut based granular ACs specifically designed for noble gas adsorption. The Nuclearcarb® 203C material was used for xenon retention in a transportable Xe monitoring system (Larson et al., 2011). Chemviron Carbon (2005) reported a Xe Henry's adsorption constant for this AC of 1.17 m<sup>3</sup>/kg at Standard Temperature and Pressure (STP). The Xe Henry's adsorption constant for the Nusorb® GXK material has been reported to be 1.39 m<sup>3</sup>/kg at room temperature and 5% Relative Humidity (R.H.) (Nucon International Inc., 2002). For both ACs, the Xe partial pressure and the gas composition at which these Xe Henry's adsorption constants were obtained were not reported. The Norit RKJ 1 material is a potassium iodide impregnated and extruded AC, which has specifically been designed for iodine trapping. This material has been investigated for iodine adsorption (Sokolenko et al., 2015), but not yet for Xe adsorption.

The selected silver-exchanged Mordenite is also commercially available. Munakata et al. (2003) showed that this type of AgZ had a higher Xe adsorption capacity than a reference AC at Xe partial pressures lower than 1000 Pa and at 0 °C. The two samples of silver-exchanged Chabazite, with different silver loadings (10-15 wt. % and 25-30 wt. % for Ag-Chabazite\_1 and Ag-Chabazite\_2 respectively), were prepared, as reported by Kuznicki et al. (2007b), on request by Extraordinary Adsorbents (2021) for the purpose of this work. Such a silver-exchanged Chabazite was reported to have a Xe adsorption capacity ranging from 0.79 to 0.88 mol/kg, depending on the synthesis process, at 1 kPa and 25 °C (Hirano et al., 2019). The Ag-ETS-10 is a commercially available AgZ. This AgZ was developed and investigated by Kuznicki et al. (2007a), who demonstrated a steep Xe adsorption isotherm reaching 0.46 mol/kg at 67 Pa and 25 °C. A sample of this AgZ was obtained for the current work; this sample is called Ag-ETS-10\_1 in the following sections. The synthesis method of the Ag-ETS-10 was further developed to improve its adsorption properties, as reported by Shi et al. (2013), leading to the development of the Ag-ETS-10\_2 sample, which is also investigated in this work. It has to be noted that Shi et al. (2013) reported a higher bulk density, *i.e.* 1.45 g/cm<sup>3</sup>, by using two different particle sizes, which is not the case for the sample used in the current work.

Kuznicki et al. (2007a); Kuznicki et al. (2007b) demonstrated the presence of silver nanoparticles on the surface of the Ag-ETS-10 and the Ag-Chabazite after synthesis. Daniel et al. (2013) showed that the observed experimental Xe adsorption isotherms on various AgZs contained two clear adsorption steps and could be represented by the sum of two independent Langmuir isotherms. The strong Xe adsorption at low Xe partial pressure in a particular silver-exchanged Pentasil, Ag-ZSM-5, was demonstrated to be likely due to the presence of silver nanoparticles on the external surface of the zeolite (Deliere et al., 2014). However, the adsorption mechanism is currently not determined (Deliere et al., 2014).

## **2.2. Xe breakthrough measurements**

An experimental set-up was developed to measure the breakthrough of stable xenon in different adsorbents. In comparison with typical volumetric or gravimetric gas adsorption instruments, used to measure adsorption isotherms, the experimental system used in this work allows to determine dynamic properties based on the Xe breakthrough curves. The set-up, presented in Figure 1, is composed of three main parts: the gas management system, the adsorption test bed, and the detection and acquisition system.

In the gas management system, the different high purity gases (He BIP®, N<sub>2</sub> BIP®, 99.9% He / 0.1% Xe BIP® and 99% N<sub>2</sub> / 1% Xe BIP®) used in the experiments were obtained from Air Products. The necessary Xe in a carrier gas mixture for an experiment is controlled by two mass-flow controllers (Voëgtlin, red-y

smart series). The Xe concentrations used in this work are ranging from 50 ppm to 1000 ppm in the carrier gas for a total pressure of 120 to 180 kPa depending on the experiments. The xenon concentration during the dissolution at fission-based MIPFs is in the range of 200 ppm, when assuming a constant release rate over one hour. This corresponds to a typical flow rate of 1000 cm<sup>3</sup>/min at Standard Ambient Temperature and Pressure and a Xe-133 activity of 4.4 10<sup>14</sup> Bq as reported by Braekers et al. (2010). A gas humidifier system can be connected in the gas management system when necessary. The humidifier consists of a double-walled concentric tube with the central pipe being a specific semi-permeable membrane (PermaPure, Nafion®), which is fed by a deionized water column. The necessary humidity level is obtained by adjusting the fraction of the flow rate passing over the humidifier as the water column height and temperature are fixed. The two relative humidity (R.H.) levels used in this work, 5 and 50%, corresponded to a dew point of  $-18 \pm 3$  °C and  $10 \pm 3$  °C respectively, for a column temperature of 21 °C. A pressure sensor (General Electric, UNIK 5000) is monitoring the pressure just after the mass flow controllers.

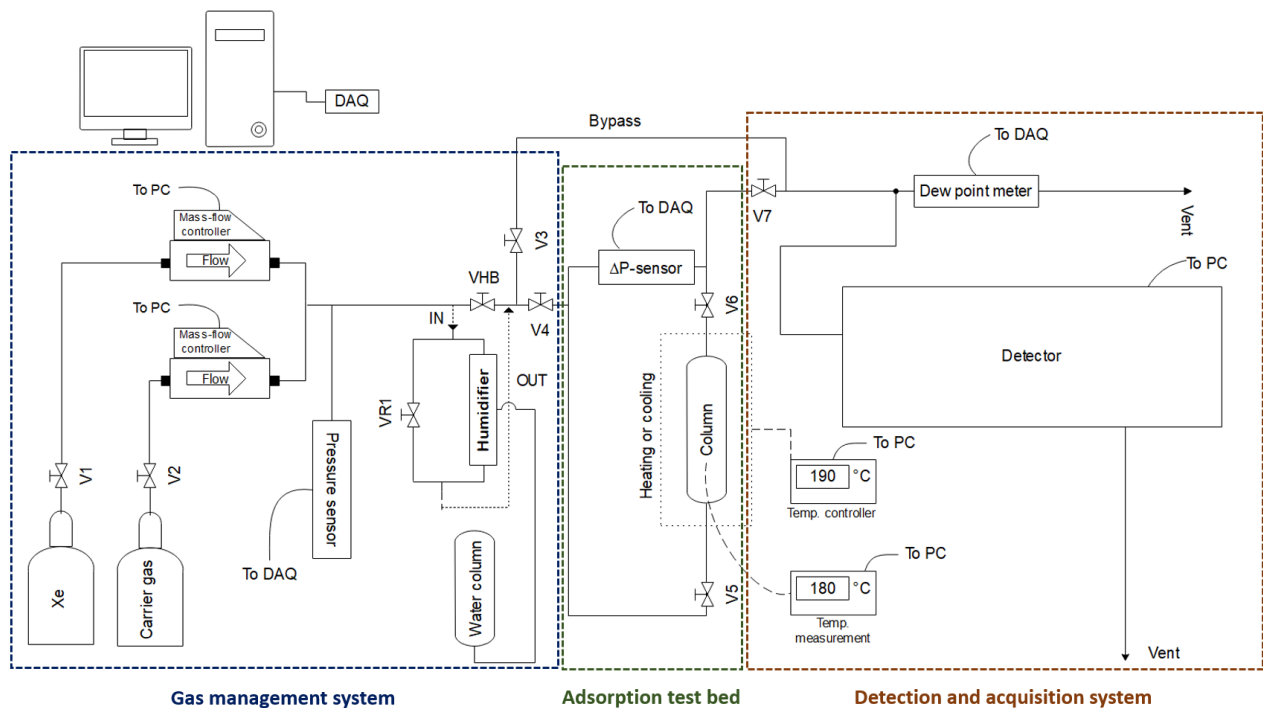


**Figure 1. Schematic representation of the experimental system for the measurement of Xe breakthrough curves. The xenon in the carrier gas mixture is obtained in the gas management system (highlighted by the blue rectangle), with the use of two mass flow controllers, fed by high purity gases, and when necessary the humidifier can be connected. The gas mixture is then sent to the adsorption test bed (highlighted by the green rectangle). Finally, the outlet of the adsorption test bed is monitored by a detector as well as a dew point meter (highlighted by the orange rectangle).**

The adsorption test bed is a stainless steel column, with a stainless steel sintered wire mesh on both ends, filled with the adsorbent to be investigated. The adsorption column is positioned vertically and the gas is fed through the upper part of the column. In this work, three different adsorption columns with different geometries were used and their characteristics are summarized in Table 2. During the filling of the adsorption column with the adsorbent, mechanical vibrations are applied on the external surface of the column to ensure a good packing of the material. For adsorbent fillings that were not fully filling the adsorption columns, glass wool is used on both ends of the column to have the adsorbent in the middle of the column and to ensure a good packing. A differential pressure sensor (KELLER, PD-23 series) is

monitoring the pressure drop across the adsorption column. The temperature of the adsorbent is continuously monitored with a thermocouple (type K) connected to a digital indicating controller (CHINO, LT300 series).

**Table 2 – Internal diameter and length of the three adsorption columns used in this work.**

Column #	Internal diameter (mm)	Internal length (mm)
C1	30	45
C2	20	80
C3	20	200

The detector system is either a Thermal Conductivity Detector (SRI Instruments, 110 GC TCD), where the carrier gas is used as reference, or a Mass Spectrometer (Hiden Analytical, HPR-20 R&D) depending on the experiments. The detector system is calibrated for Xe at least every week in the range of Xe concentrations in the corresponding carrier gas, necessary for the experiments. The dew point sensor (Michell, Easidew Online) is monitoring the dew point in parallel of the detector system.

Before each breakthrough experiment, the adsorbent is regenerated at the desired temperature, typically 200 °C, under a helium or nitrogen flow, depending on the carrier gas used for the following experiment. For the Ag-Chabazite\_2 sample specifically, a temperature of 160 °C was used, as a decrease in Xe adsorption capacity during successive adsorption/desorption cycles was observed at a regeneration temperature of 200 °C. The process is controlled by a temperature controller (West Control Solutions, KS20) in combination with a thermocouple (type K) on the external surface of the column. The temperature set point was maintained until no xenon could be observed in the detector. The heating system is either a 180 W e-glass textile heating wire (Eltherm, ELK-HS) wrapped around the column or a 1200 W infrared lamp (Heraeus, SW/1200W), with a gold reflector, directed towards the column.

The following parameters are continuously recorded on a PC: flow rate on both mass flow controllers, inlet pressure, pressure drop across the adsorption column, temperature of the test bed and dew point. All values reported in this work correspond to the median value over the duration of the experiments.

From the experiments, two parameters were directly extracted: the Xe adsorption capacity and retention time. The adsorption capacity ( $q$ ) corresponds to the amount of xenon retained in the material until full breakthrough ( $t_b$ ), as shown in Equation 1. It is determined based on calibrations made on beforehand with the relevant xenon concentrations ( $C$ ). The mass of adsorbent ( $M$ ) is measured with a mass balance (METTLER, AE240) after the set of experiments performed in the adsorption column, which always ended by a desorption. The median flow rate ( $F$ ) over the duration of the experiment is used in Equation 1. For the measurement of Xe adsorption isotherms, the Xe adsorption capacity at each Xe partial pressure is measured successively. The retention time ( $t_{XX\%}$ ), which can be defined at any percentage of the breakthrough curve (XX%), is corresponding to the time required to have a certain percentage of breakthrough of xenon (*i.e.* percentage of the inlet concentration).

$$q = \frac{F \int_0^{t_b} (C_{inlet} - C_{outlet}) dt}{M} \quad \text{Equation 1}$$

In addition, the notion of Mass Transfer Zone (MTZ) is used to quantify the overall mass transfer kinetics (diffusion, dispersion and adsorption-desorption) of Xe during each experiment, which is in the current work defined as the zone going from 10% to 90% breakthrough ( $t_{10\%}$  and  $t_{90\%}$ ). This is the percentage of the

adsorbent bed where active adsorption occurs. The relative length of this zone is calculated based on the definition in Zhou et al. (2011). The definition of the MTZ percentage used in the current work is given in Equation 2.

$$MTZ (\%) = \frac{2(t_{90\%}-t_{10\%})}{(t_{90\%}+t_{10\%})} \cdot 100 \% \quad \text{Equation 2}$$

The uncertainty on the Xe adsorption capacity and retention time at 10% of the overall experimental system was evaluated through ten successive measurements of breakthrough curves on a sample of Nusorb® GXK in the same conditions, which are given in Supplementary material Table S1. The average adsorption capacity in these conditions was  $1.2 \cdot 10^{-2}$  mol/kg and the minimum and maximum values were  $1.1 \cdot 10^{-2}$  mol/kg (-8.3%) and  $1.3 \cdot 10^{-2}$  mol/kg (+8.3%) respectively. The average retention time at 10% was 36 minutes and the minimum and maximum values were 35 (-2.8%) and 39 minutes (+8.3%) respectively. The average MTZ percentage was 66% and the minimum and maximum values were 63% (-4.0%) and 70% (+6.6%) respectively. This can be considered as a worst-case uncertainty as the same sample was used throughout the ten breakthrough curves and a desorption step was performed in between the adsorption runs so that a potential degradation of the material cannot be excluded. An uncertainty of  $\pm 10\%$  is used for the reported Xe adsorption capacities, retention times at 10%, and MTZ percentages.

### 2.3. Gamma irradiation

A sample of Ag-ETS-10\_2 was irradiated in the BRIGITTE (Big Radius Installation under Gamma Irradiation for Tailoring and Testing Experiments) gamma irradiation facility at SCK CEN. The BRIGITTE irradiation facility is described in Fernandez et al. (2002). The sample, with a mass of 22 g, was irradiated for 50 hours in this facility under a constant and homogeneous gamma absorbed dose rate of 20 kGy/h, resulting in a total gamma absorbed dose of 1 MGy.

## 3. Results and discussion

The comparison of the Xe adsorption capacity of the studied adsorbents is presented and discussed in subsection 3.1. In the same subsection, the effect of moisture on the Xe adsorption capacity and a specific comparison of the two Ag-ETS-10 samples is given as well. In subsection 3.2, the applicability of the Ag-ETS-10 material in conditions relevant for radioxenon mitigation in fission-based medical isotope production facilities is discussed.

### 3.1. Comparison of Xe adsorption on the different adsorbents

Xe adsorption capacities at about 6.5, 13, 65 and 130 Pa at room temperature, in Xe/He and Xe/N<sub>2</sub> mixtures, were measured on the **different AC and AgZ adsorbents**, except on the Ag-ETS-10\_1 that is discussed separately hereafter. The detailed experimental conditions can be found in Supplementary material Table S2A for helium and in Table S2B for nitrogen. The resulting Xe adsorption capacities are presented in Figure 2a for ACs and in Figure 2b for AgZs. Assuming a linear adsorption isotherm for the three ACs, the Xe Henry's adsorption constant is 1.15, 0.947 and 0.725 m<sup>3</sup>/kg in He, and 0.688, 0.635 and 0.781 m<sup>3</sup>/kg in N<sub>2</sub> for Nusorb® GXK, Nuclearcarb® 203C and Norit RKJ1 respectively. For Nusorb® GXK and Nuclearcarb® 203C, there is a clear decrease in Xe adsorption when going from He to N<sub>2</sub> whereas for Norit RKJ1 the difference is within the uncertainties. These results indicate that there is no significant Xe/N<sub>2</sub> adsorption competition at room temperature in the range of partial pressures investigated for Norit RKJ1

whereas there is a significant Xe/N<sub>2</sub> adsorption competition in the two other ACs. When He is used as carrier gas, Nusorb® GXK clearly offers the highest Xe adsorption capacity whereas when nitrogen is used as carrier gas, the three ACs offer a similar Xe adsorption capacity. The highest Xe Henry's adsorption constant for Nusorb® GXK is about 17% lower than the one reported at room temperature by Nucon International Inc. (2002) for which the carrier gas and Xe partial pressure were not reported. The highest Xe Henry's adsorption constant for Nuclearcarb® 203C is about 20% lower than the one reported at STP by the producer with, again, an unknown gas composition and Xe partial pressure (Chemviron Carbon, 2005). For this AC, the difference in temperature could explain the lower Xe Henry's adsorption constant.

For all AgZs, there is a significant Xe/N<sub>2</sub> adsorption competition as all Xe adsorption capacities measured in nitrogen were lower than the ones measured with helium. The order, with regard to the highest Xe adsorption capacity, on each AgZ is Ag-ETS-10\_2 > Ag-Chabazite\_2 > Ag-Chabazite\_1 > Ag-Mordenite. The Xe adsorption capacity at about 65 Pa on the Ag-ETS-10\_2 sample is 0.48 mol/kg at room temperature, which is very similar to the 0.46 mol/kg reported by Kuznicki et al. (2007a) in the same conditions on an Ag-ETS-10 sample. However, as shown in the following paragraphs, the Ag-ETS-10\_2 sample has a higher Xe adsorption capacity, by about 20%, than the Ag-ETS-10\_1 sample. The latter corresponds to a similar sample as the one reported in Kuznicki et al. (2007a). The highest Xe adsorption capacity measured on the Ag-Chabazite samples was 0.24 mol/kg at about 130 Pa on the Ag-Chabazite\_2 sample. Assuming a Langmuir type adsorption isotherm, the extrapolated Xe adsorption capacity at 1 kPa on this sample would be 0.53 mol/kg, which is lower than the reported values of 0.79 to 0.88 mol/kg at 1 kPa by Hirano et al. (2019). Differences in the isotypic chabazite structure, the activation temperature and silver exchange likely explain the difference (Fujie et al., 2010; Saxton et al., 2010). The ratio of the Xe adsorption capacity of Ag-Chabazite\_2 to Ag-Chabazite\_1 ranged from 1.5 to 2.0 for Xe/He - and from 2.0 to 2.4 for Xe/N<sub>2</sub> mixtures. The results on both Ag-Chabazite samples clearly indicate that the Xe adsorption capacity is a function of silver loading. This is in agreement with the observations made by Daniel et al. (2013) on Pentasil-type zeolites. Finally, the Ag-Mordenite had the lowest Xe adsorption capacity of all adsorbents investigated. The Xe adsorption capacity in He at about 130 Pa and room temperature was  $4.3 \cdot 10^{-3}$  mol/kg for this sample, which is well below the Xe adsorption capacity measured by Munakata et al. (2003) of about 0.3 mol/kg at about 100 Pa and 0 °C on a Ag-Mordenite. The difference in temperature is clearly part of the explanation for this difference. However, it is unlikely that the Xe adsorption capacity would increase by about two orders of magnitude when going from room temperature to 0 °C. Beyer and Jacobs (1982) showed that silver nanoparticles are only formed on Ag-Mordenites under an external reducing agent and at a sufficiently high temperature. As no information on the synthesis process of the Ag-Mordenite, studied in this work, is available, it is possible that the used synthesis process did not efficiently result in silver nanoparticles and could be part of the cause for the observed difference.

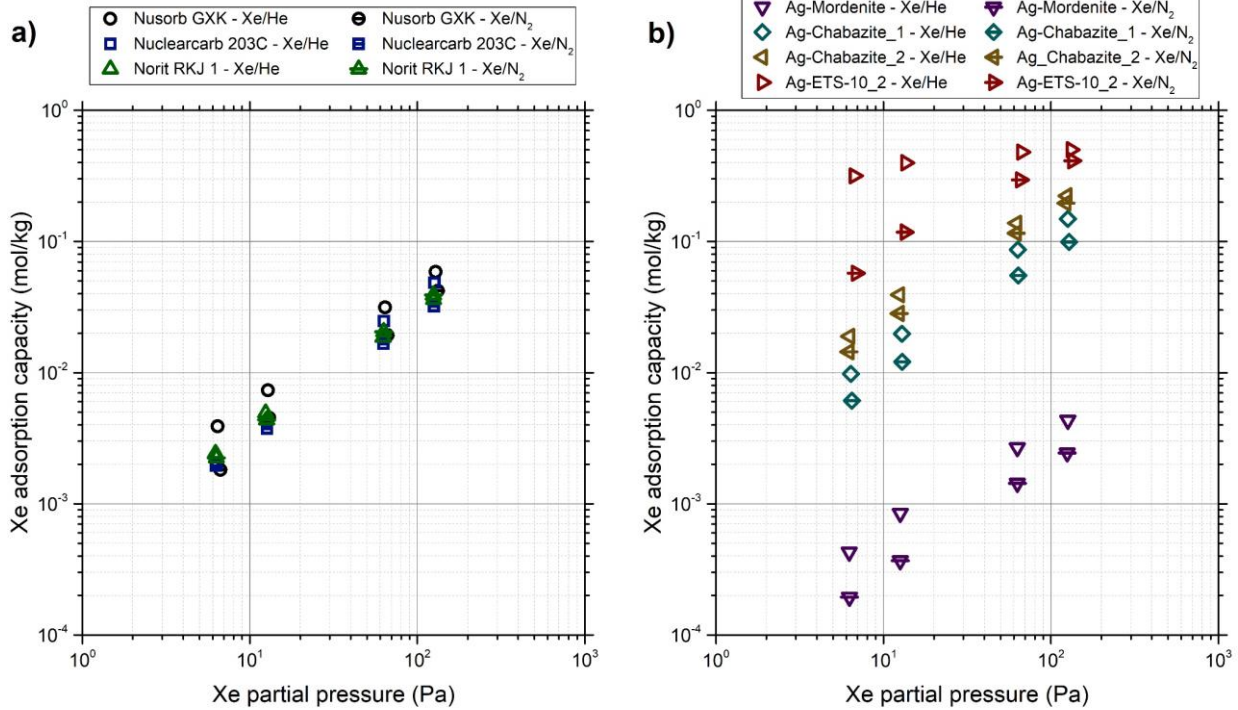


**Figure 2. Overview of the measured Xe adsorption capacity  $q_{Xe}$  (mol/kg), at 50, 100, 500 and 1000 ppm Xe in helium and nitrogen, on the different adsorbent materials: a) ACs and b) AgZs.**

The benefit of using the Ag-ETS-10\_2 sample over a nuclear grade AC such as Nusorb® GXX for Xe adsorption, both in He and N<sub>2</sub>, is clear from Figure 2. The Xe adsorption capacity at 6.5 and 130 Pa in Xe/He increases by a factor 81 and 8.5 respectively; whereas in Xe/N<sub>2</sub> it increases by a factor 31 and 10 respectively. As the available space for a Xe trapping system in an existing facility could be limited, the Xe adsorption capacity per unit of volume is in this case a more crucial factor. As shown in Table 1, the density of the Ag-ETS-10\_2 sample is about twice the density of Nusorb® GXX, which, in terms of volume, further increases the adsorbed amount of Xe by a factor two. The comparison in terms of volume on the amount of Xe retained in the material, the Xe retention time at 10 and 90%, and the MTZ percentage is highlighted by the ratio of these quantities in Table 3 for two Xe concentrations in both Xe/He and Xe/N<sub>2</sub> mixtures. The detailed experimental conditions for the underlying breakthrough curves can be found in Supplementary material Table S3. As can be seen in Table 3, the ratio for the adsorbed amount of Xe ranges from 17.9 up to 185 depending on the Xe concentration and carrier gas. More importantly, the ratio for the retention time at 10% is even higher with values ranging from 20.2 up to 211. In practice at 50 ppm Xe in He, the same volume of adsorbent can be used for a time period that is 211 times longer. The lower MTZ percentage in the Ag-ETS-10\_2 sample compared to Nusorb® GXX indicates a faster overall mass transfer kinetic and thus a relatively sharper breakthrough.

**Table 3 – Ratio of the adsorbed amount of Xe ( $n_{Xe}$ ), Xe retention time at 10 and 90% and MTZ percentage of the Ag-ETS-10\_2 sample on the Nusorb® GXX sample with He and N<sub>2</sub> at two Xe concentrations.**

Xe con. (ppm)	Carrier gas	Ratio Ag-ETS-10_2/Nusorb® GXX			
		$n_{Xe}$	$t_{10\%}$	$t_{90\%}$	MTZ percentage
50	He	185	211	155	0.6

<b>1000</b>	<b>He</b>	18.2	20.2	15.8	0.6
<b>100</b>	<b>N<sub>2</sub></b>	43.4	49.9	39.4	0.7
<b>1000</b>	<b>N<sub>2</sub></b>	17.9	23.7	14.0	0.2

The Xe breakthrough curves of Ag-ETS-10\_1 and Ag-ETS-10\_2 were compared, with a gas mixture of 1000 ppm Xe/He at room temperature, to determine the improvement in Xe adsorption of the new sample, produced with a **new synthesis method**. The detailed experimental conditions can be found in Supplementary material Table S4. The resulting average Xe adsorption capacity was 0.61 mol/kg for the Ag-ETS-10\_1 sample and 0.72 mol/kg for the Ag-ETS-10\_2 sample, corresponding to a relative increase of 18%. In addition, it has to be noted that the density of the Ag-ETS-10\_2 sample increased by 22.2 % compared to the Ag-ETS-10\_1 sample, which further increases the Xe adsorption capacity per unit volume of adsorbent. The resulting average Xe retention time at 10% per unit mass of adsorbent was 21 min/g for the Ag-ETS-10\_1 sample and 26 min/g for the Ag-ETS-10\_2 sample, corresponding to a relative increase of 24%. These increases are significant compared to the 10% uncertainty on these measurements. Shi et al. (2013) reported a relative increased retention time per unit mass of material of 28 % for Ar for a high density Ag-ETS-10 compared to the regular Ag-ETS-10. This is in agreement with the results obtained in the current work for Xe. In Figure 3, for each sample, one of the obtained breakthrough curves is presented, normalized with regard to the Xe inlet concentration. For this comparison, the x-axis is rescaled by dividing the time by the mass of each sample, as the masses were not exactly the same (25.9 g and 26.8 g for the Ag-ETS-10\_1 and Ag-ETS-10\_2 samples respectively). The average MTZ percentage corresponded to 38% and 20% of the bed length for the Ag-ETS-10\_1 and Ag-ETS-10\_2 samples respectively indicating a significantly smaller MTZ percentage in the Ag-ETS-10\_2 sample. The Xe breakthrough curve on the Ag-ETS-10\_2 sample follows a logistic function ('S' shape profile) around the retention time at 50% as expected for ideal breakthrough curves, whereas the breakthrough curve on the Ag-ETS-10\_1 sample does clearly not follow a logistic function. The lower slope at the beginning of the breakthrough curve on the Ag-ETS-10\_1 sample is due to a slower overall mass transfer kinetic, which is likely the result of the different binder. Even more interesting is the sharper breakthrough at the end of the curve for the Ag-ETS-10\_1 sample, which would indicate a preferential channel with less adsorbent encountered by the gas at the end of the adsorbent bed. This could be due to an imperfect packing of the Ag-ETS-10\_1 sample, with an inhomogeneous packing density along the adsorbent bed, as highlighted during other experiments and discussed in Section 3.2.7. The higher Xe adsorption capacity and retention time at 10% clearly demonstrate that it is still possible to further optimize the adsorption materials for the capture of xenon and thus decrease the volume of material required for a defined amount of xenon to be captured.

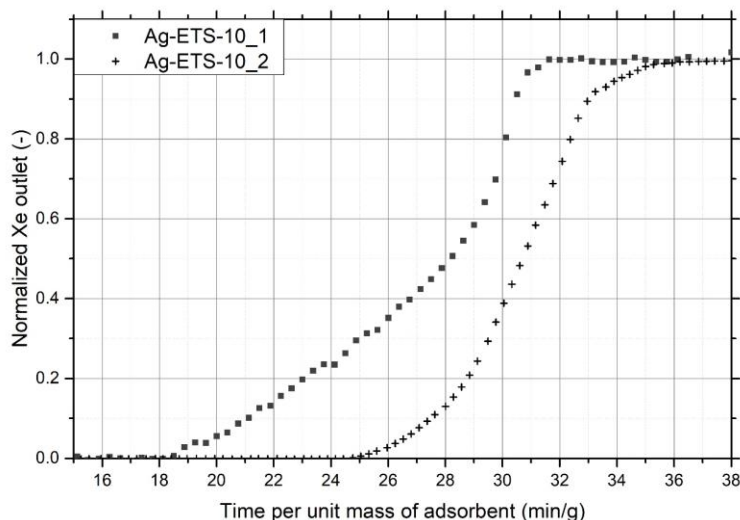


**Figure 3. Normalized Xe breakthrough curves obtained on the Ag-ETS-10\_1 (■) and the Ag-ETS-10\_2 (+) samples. The x-axis is rescaled with the mass of adsorbent, as these were slightly different.**

As moisture can still be present in the gas stream going from the production process to a potential radionuclide mitigation system, **the effect of moisture** on the Xe adsorption capacity for the different materials was investigated. The adverse impact of moisture on iodine adsorption in AgZs has been shown in the past (Nan, 2017). However, the effect of moisture content in the gas stream on the Xe adsorption in AgZs, has to the best of our knowledge, not yet been reported. For this purpose, two moisture contents were investigated: 5% and 50% Relative Humidity (R.H.). These are compared with a run in dry conditions. Before the experiment, the sample was fully regenerated and then the chosen moisture content was maintained until the full Xe breakthrough was observed. The obtained Xe adsorption capacity, for a mixture of 250 ppm Xe/N<sub>2</sub> at room temperature, for all adsorbents, except for Ag-ETS-10\_1, with these three moisture levels in the inlet gas stream is shown in Figure 4. The detailed experimental conditions can be found in Supplementary material Table S5. As can be seen in Figure 4, a significant decrease in Xe adsorption capacity was observed for the Ag-ETS-10\_2 and Ag-Chabazite\_2 samples at 50% R.H. The Xe adsorption capacity decreased by a factor 31 when going from dry conditions to 50% R.H. on Ag-ETS-10\_2 whereas it decreased by a factor 6.6 on Ag-Chabazite\_2. A decrease in Xe adsorption coefficient on coconut-based AC was demonstrated by Underhill et al. (1986) when the AC was equilibrated with the moisture content in advance. This is clearly different from the methodology used in the current work, as it is here considered that the adsorbent is fully desorbed before each use. In this case, the water uptake is clearly not sufficient to decrease the Xe adsorption capacity on the ACs investigated.

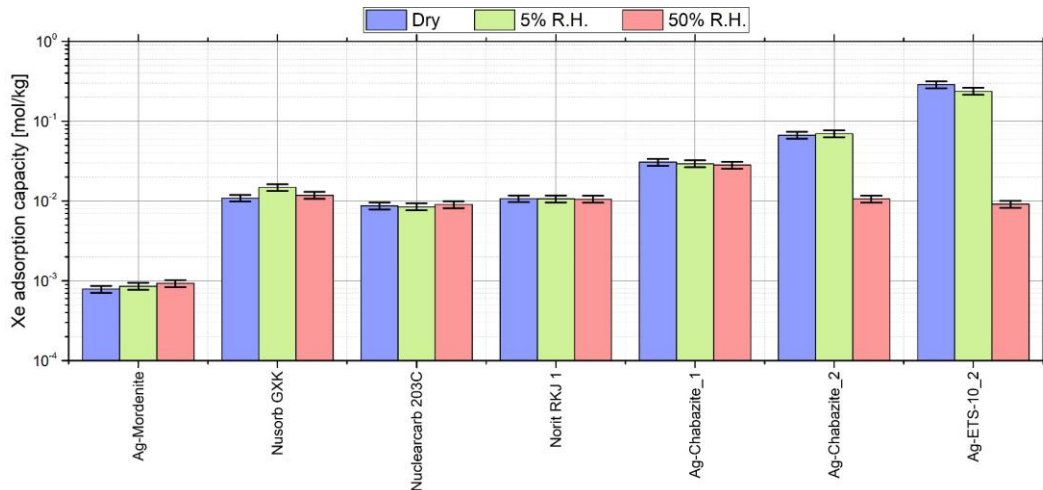


**Figure 4 - Evolution of the Xe adsorption capacity as a function of the moisture content in the gas stream, for a mixture of 250 ppm Xe in nitrogen at room temperature, for each material.**

The effect on the Xe retention time at 10%, for the Ag-ETS-10\_2 sample, was much more limited than on the Xe adsorption capacity as it decreased only by a factor 2.3. This is highlighted in Figure 5, where the normalized Xe breakthrough is shown for the three moisture contents on the Ag-ETS-10\_2 sample. As can be seen in the figure, the Xe breakthrough at 10% is occurring significantly faster at 50% R.H. but the main loss in Xe adsorption capacity is in fact due to the strong roll-up of Xe, as Xe is displaced from the adsorption sites by water molecules (Carter and Husain, 1974). During the roll-up, 92% of the adsorbed Xe is released from the material. Such a roll-up of Xe was also observed on the Ag-Chabazite\_2 sample at 50% R.H., for which the retention time decreased by a factor 1.3. A Xe roll-up is critical for radionuclide mitigation systems, as this would lead to a large Xe release. The moisture content when using these AgZs should thus be well controlled to avoid this situation.

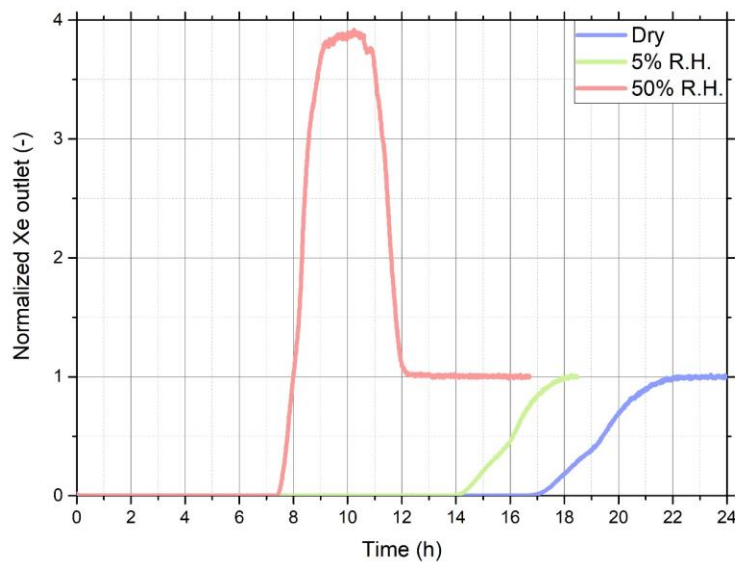


**Figure 5 – Comparison of the normalized Xe breakthrough curves obtained on the Ag-ETS-10\_2 sample in dry conditions, and at 5% and 50% R.H.**

### **3.2. Applicability of Ag-ETS-10 for radionuclide mitigation**

As shown in the previous section, Ag-ETS-10 is a promising adsorbent to support the reduction of radionuclide emissions of fission-based MIPFs by providing a more efficient Xe adsorption per unit of volume of adsorbent compared to all ACs and all other AgZs considered in this work. The applicability of Ag-ETS-10 for this specific industrial setting is further considered in this section. The effect of inlet concentration, column geometry, flow rate and temperature on the Xe breakthrough curves was investigated. In addition, the durability of Ag-ETS-10\_2 against gamma irradiation was explored. Finally, the regeneration of the material and its durability against desorption/adsorption cycles were investigated.

#### **3.2.1. Effect of inlet concentration**

The effect of the inlet concentration on the Xe adsorption capacity of Ag-ETS-10\_2 was shown in Section 3.1. The Xe adsorption isotherm of this sample (Figure 2) clearly indicated a Langmuir type adsorption isotherm, as the material started to get saturated with Xe at the highest Xe partial pressures. In comparison, Nusorb had a linear adsorption isotherm in the Xe partial pressure range investigated. In Figure 6a for Ag-ETS-10\_2 and in Figure 6b for Nusorb, one of the measured Xe breakthrough curves after desorption, resulting in Figure 2, is shown for both 100 - and 1000 ppm Xe in N<sub>2</sub> at room temperature. The detailed experimental conditions for these breakthrough curves can be found in Supplementary material Table S6. For Nusorb, both breakthrough curves (Figure 6b) are overlapping each other within the 10% uncertainty as expected from the linear adsorption isotherm.

For the Ag-ETS-10\_2 sample however, the Xe adsorption capacity increased by a factor 3.5 when going from 100 ppm to 1000 ppm Xe in N<sub>2</sub> at room temperature. From Figure 6a, it can clearly be observed that the slope of the curve is very different depending on the Xe concentration. On average, the MTZ percentage represented 50 % and 16 % of the bed length at 100 and 1000 ppm Xe respectively. The Xe breakthrough at 1000 ppm Xe has a very sharp breakthrough profile, which indicates a very fast overall mass transfer kinetic. Whereas the Xe breakthrough at 100 ppm Xe has a significantly flatter slope compared to the one at 1000 ppm Xe, which in turn indicates a slower overall mass transfer kinetic. As the breakthrough curves were obtained on the same amount of material, geometry, flow rate and other experimental conditions, it can only be concluded that the overall mass transfer kinetic has a concentration dependency in this material. Such an observation was also made by Puertolas et al. (2010) with propene breakthrough curves on a ZSM-5 zeolite, having a Langmuir type adsorption isotherm, where the slope increased with increasing concentrations. The “trough” in the Xe breakthrough curve at 100 ppm could be due to some imperfections in the packing of the adsorbent in the test bed. Such imperfections are discussed further in Section 3.2.7. The results are clearly highlighting that the design of a Xe adsorbent bed, with adsorbents having a Langmuir adsorption isotherm, should take into consideration the specific Xe concentration of the process, to assess the dimensions of the adsorbent bed correctly.

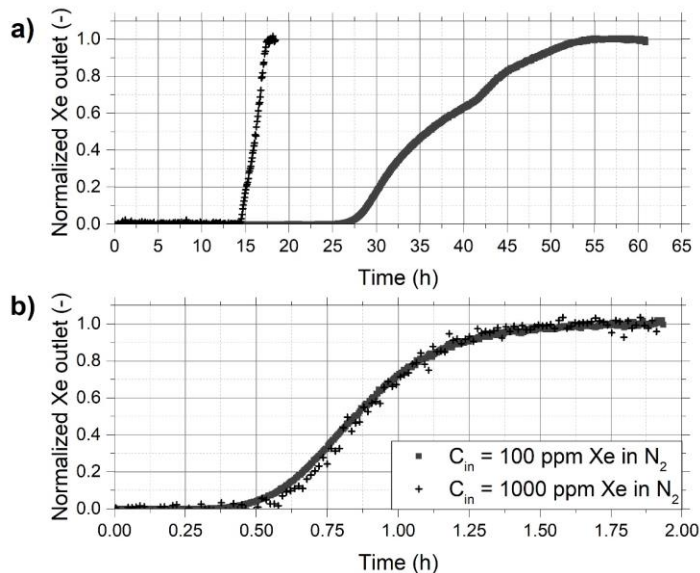


**Figure 6 - Normalized Xe breakthrough curve for a) a 100 ppm Xe in N<sub>2</sub> mixture (■) and a 1000 ppm Xe in N<sub>2</sub> mixture (+) at room temperature in the Ag-ETS-10\_2 adsorbent and b) a 100 ppm Xe in N<sub>2</sub> mixture (■) and a 1000 ppm Xe in N<sub>2</sub> mixture (+) at room temperature in the Nusorb adsorbent.**

### 3.2.2. Effect of column geometry

The effect of the Length to Diameter ratio (L/D) of the adsorption column on Xe adsorption was investigated by measuring Xe breakthrough for two different ratios, 1.1 and 3.8, in a mixture of 1000 ppm Xe in He at room temperature and for the same mass of adsorbent. In practice, the same Ag-ETS-10\_2 sample was used in adsorption columns C1 (L/D 1.1) and C2 (L/D 3.8). Detailed experimental conditions can be found in Supplementary material Table S7. The resulting Xe breakthrough curves are shown in Figure 7. The Xe adsorption capacity obtained with C1 was 0.69 mol/kg and with C2 it was 0.72 mol/kg. These values are within the uncertainties of the measurement and are in agreement with the expectations. As the adsorption capacity is measured at equilibrium, the geometry of the adsorption column should not affect the adsorption capacity. The difference between both breakthrough curves is thus on the Xe adsorption kinetic which is, as can be seen in the figure, significantly different. The MTZ percentage represented 90 % and 27 % of the bed length for C1 and C2 respectively. The retention time at 10% went from 5.4 hours in C1 to 9.4 hours in C2. The increase due to the larger L/D ratio is thus 72% and provides a significant difference in volume required for a certain retention time. The smaller slope for the smaller L/D ratio indicates a slower overall mass transfer kinetic, whereas the steeper slope for the higher L/D ratio indicates in turn a faster overall mass transfer kinetic. The decrease in bed diameter going from C1 to C2 gives a higher superficial velocity, and thus a shorter contact time with the adsorbent. The MTZ percentage is expected to increase with increasing superficial velocity as discussed in Section 3.2.3. The current results indicate however an opposite trend; this is likely due to a better flow distribution in C2 compared to C1. This is explained by the use of the same inlet-pipe diameter for both columns, which gives rise to a smaller velocity gradient in the transverse direction in C2 compared to C1. The earlier breakthrough in C1 is due to a smaller volume of adsorbent in the region where the velocity is the highest whereas the longer time required to reach equilibrium is due to the lower velocity in the region along the column wall. The flow distribution in the adsorbent is an aspect that should be considered with care in the design of Xe trapping systems. The effect of flow rate in a fixed column geometry is further discussed in the following section. The steeper slope at

the end of the Xe breakthrough curve in C1 could be due to some imperfections in the packing of the material in the adsorption column as discussed further in 3.2.7.

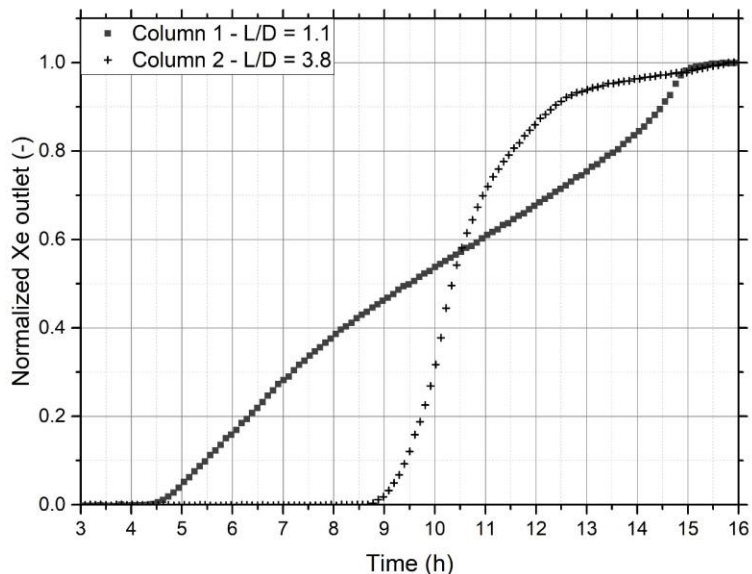


**Figure 7** –Normalized Xe breakthrough curves, with 1000 ppm Xe in He at room temperature, obtained with column C1 (■) and C2 (+) filled with the same Ag-ETS-10\_2 sample.

### 3.2.3. Effect of flow rate

The effect of the flow rate on Xe adsorption in the Ag-ETS-10\_2 sample was investigated by measuring the Xe breakthrough at four flow rates, *i.e.* 280, 400, 1400 and 2800 cm<sup>3</sup>/min, in the same column. All other conditions were kept constant. The detailed experimental conditions can be found in Supplementary material Table S8. The Xe adsorption capacity varied between 0.46 and 0.55 mol/kg, which is perfectly within the 10% uncertainty on the average value obtained in Figure 2 for this Xe partial pressure. There is thus no significant effect on the Xe adsorption capacity, indicating that equilibrium was reached within the material for all flow rates. The Xe breakthrough curves obtained at these flow rates are shown in Figure 8a, where the x-axis has been rescaled with the flow rate for visualisation purposes and is thus representing the volume of gas processed in the adsorbent bed. The retention volume at 10% breakthrough was 0.190, 0.183, 0.165 and 0.161 m<sup>3</sup> for 280, 400, 1400 and 2800 cm<sup>3</sup>/min respectively, which indicates a slower overall mass transfer kinetic when the flow rate increases. For this aspect, the superficial velocity of the gas inside the adsorption column is a critical factor. The superficial velocity was 1.5, 2.1, 7.4 and 15 cm/s for a flow of 280, 400, 1400 and 2800 cm<sup>3</sup>/min respectively. As the adsorbent filling in the column was kept constant, this increased velocity resulted in a shorter contact time with the adsorbent inside the column. The results clearly show that the adsorption sites are much more difficult to reach at a high superficial velocity resulting in a longer time duration, and a larger MTZ percentage, to reach equilibrium. The MTZ percentage of the bed length as a function of superficial velocity is shown in Figure 8b. In this figure, a linear equation was fitted. The resulting R-squared is 0.85 indicating indeed a linear correlation in this range of superficial velocity. Such a linear relationship was shown numerically by Rezaei and Webley (2009) for CO<sub>2</sub>/N<sub>2</sub> separation on different adsorbent structures. More surprising is the change of slope in each breakthrough curve occurring at about 40-50% breakthrough. This could again be due to an inhomogeneous packing of the material in the adsorption test bed as will be discussed in Section 3.2.7. Another possible cause for this

change in slope could be related to the two distinct adsorption sites in these AgZs, one adsorption site for the zeolite and a second one for the silver nanoparticles (Deliere et al., 2014), which could have different mass transfer properties.

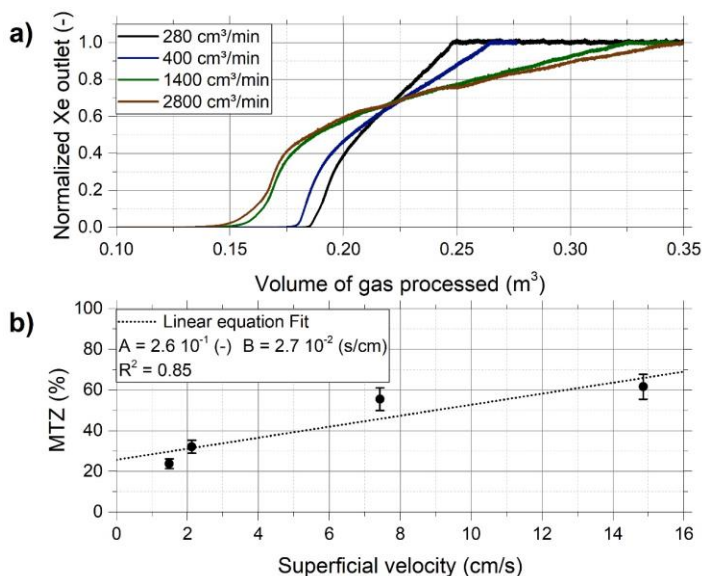


**Figure 8 – a) Normalized Xe breakthrough curves, in function of volume of gas processed, obtained on the Ag-ETS-10\_2 sample with a flow rate of 280, 400, 1400 and 2800 cm<sup>3</sup>/min and b) Mass Transfer Zone percentage with regard to the bed length as a function of superficial velocity together with the linear fit.**

### 3.2.4. Durability against gamma irradiation

Xe adsorption capacity, retention time at 10%, and MTZ percentage, were measured during a 1000 ppm Xe in He adsorption run at room temperature before and after a gamma irradiation of 1 MGy on the Ag-ETS-10\_2 sample. Xe breakthrough curves before and after irradiation are compared in Figure 9. The detailed experimental conditions can be found in Supplementary material Table S9. The average Xe adsorption capacity, measured after irradiation, was 0.63 mol/kg, which is 6% lower than the average Xe adsorption capacity before irradiation. The average Xe retention time at 10% measured after irradiation was 8.8 h, which is 6% higher than before irradiation. The values are thus clearly within the uncertainties and no significant effect on Xe adsorption was observed. On the other hand, the MTZ percentage represented 27% of the adsorbent after irradiation whereas it represented 39% before irradiation. The decrease in MTZ percentage is clearly significant. However, as will be discussed in Section 3.2.7., this is likely related to the packing density of the material inside the adsorption column, resulting in an inhomogeneity of the packing, having a significant effect on the MTZ percentage, which was observed before irradiation as well as shown further in Figure 11b. Accordingly, no effect on the Xe adsorption properties could be observed after the 1 MGy gamma irradiation. To the best of our knowledge, this study is the first investigation on the durability of this AgZ against gamma irradiation.

As shown by Saey et al. (2010a) and Lee et al. (2016), the major contributor to the radioxenon releases from fission-based MIPFs is Xe-133 and the typical Xe-133 activity released after the dissolution of irradiated targets is in the range of  $10^{14}$  Bq. By considering the isotopic power of  $2.14 \cdot 10^{-14}$  W/Bq from beta - and  $7.39 \cdot 10^{-15}$  W/Bq from gamma decay for Xe-133 (JEFF-3.1 Nuclear Data Library), this would yield a power of 2.14 - and 0.739 J/s from beta and gamma decay respectively. The exploration of the durability of the Ag-

ETS-10\_2 sample was performed on a sample of 21.6 g. Considering this mass and that all beta and gamma radiation would be absorbed in the material, this would yield in turn an absorbed dose of 0.36 - and 0.12 MGy/h or about 1 MGy for 3 - and 8 hours of operation for beta and gamma radiation respectively. This means that the current exploration of the durability of the material would need to be extended not only to consider beta radiation but also to a higher absorbed dose in the future to ensure its durability to radiation in operational conditions at fission-based MIPFs.

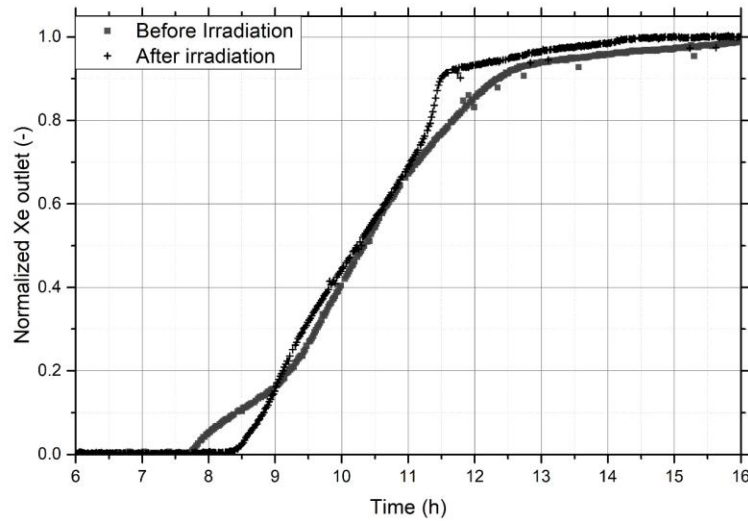


**Figure 9. Normalized Xe breakthrough curves, for a mixture of 1000 ppm Xe in He at room temperature, obtained before (■) and after (+) the gamma irradiation with an absorbed dose of 1 MGy on the Ag-ETS-10\_2 sample.**

### 3.2.5. Xe adsorption at 60 °C

Radioactive decay of the different Xe isotopes could result in a heat build-up in the material. If not sufficiently dissipated, this could decrease the adsorption capacity as adsorption is an exothermal process where the adsorption capacity decreases with increasing temperature following a van 't Hoff equation (Ruthven, 1984). In order to assess this potential decrease, Xe breakthrough curves with 1000 ppm Xe in He at 60 °C were evaluated and compared to these obtained at room temperature. 60 °C is considered as the upper level for operation without dedicated cooling during adsorption. The detailed experimental conditions can be found in Supplementary material Table S10. The obtained average Xe adsorption capacity, retention time at 10% and MTZ percentage are shown in Table 4. Xe adsorption capacity decreased by a factor 2.5 from room temperature to 60 °C, whereas Xe retention time decreased by a factor 1.3. The MTZ percentage did not change between the different experiments, which were performed with the same filling and thus the same packing. The reduction in adsorption capacity and retention time could thus have a significant effect and could potentially cause an earlier breakthrough if the radioactive decay would result in an increase in temperature during operation.

**Table 4 – Comparison of the average temperature, inlet pressure, Xe adsorption capacity and retention time at 10%, and MTZ percentage on the Ag-ETS-10\_2 sample at room temperature and at 60 °C for the experiments with 1000 ppm Xe in He.**

T (°C)	P (kPa)	q <sub>Xe</sub> (mol/kg)	t <sub>10%</sub> (h)	MTZ (%)
23	174	0.61	9.1	20%
60	173	0.25	7.1	20%

### 3.2.6. Regeneration conditions

The regeneration of AgZs without any loss of Xe adsorption capacity is crucial, as these materials are far more expensive than typical ACs. In addition, an efficient regeneration process is needed to minimize the operational cost of a Xe trapping system. Accordingly, the regeneration of the Ag-ETS-10\_2 sample was investigated at three desorption temperature set points, *i.e.* 150 °C (internal temperature: 136 °C), 200 °C (internal temperature: 171 °C) and 250 °C (internal temperature: 221 °C), under a continuous helium flow. The detailed experimental conditions of these desorption runs, together with their subsequent adsorptions, are given in Supplementary material Table S11. The desorption curves, normalized to the maximum Xe concentration obtained at 250 °C, for these experiments are shown in Figure 10. A heating ramp of 2 °C/min was used and once the temperature set point was reached, it was maintained for 3 hours before shutting down the heating element. As can be seen in the figure for the desorption run at 250 °C, the maximum of the desorption was reached before getting at 250 °C (at about 200 °C) and a back-fall to 1% of the maximum was obtained 0.6 hours after reaching the temperature plateau. For the run at 200 °C, the maximum was reached at the set point, as could have been expected from the run at 250 °C, the desorption peak is however wider and falls back to 1% of the maximum only after 2.3 hours. Finally, for the run at 150 °C, the maximum is reached at the set point temperature, it would most likely have increased further if the temperature set point was higher as shown in the previous runs, and the peak is again broader and does not fall back to 1% of its maximum before the end of the temperature plateau. This could, of course, be improved by a longer heating duration or eventually a higher flow rate.

Xe adsorption capacities during the subsequent adsorptions with 1000 ppm Xe in He at room temperature were 0.73, 0.73 and 0.70 mol/kg after the desorption at 250, 200 and 150 °C respectively. The Xe retention time at 10% during these adsorptions was 9.4, 9.5 and 9.2 hours in the same order. Finally, the MTZ percentage represented 29, 27 and 24% of the bed length, again in the same order. According to the uncertainties, there are no significant variations in these parameters. This is indicating that, even though the desorption at 150 °C did not fall back to 1% of its maximum during the temperature plateau, the desorption was still sufficient to recover the Xe adsorption capacity.

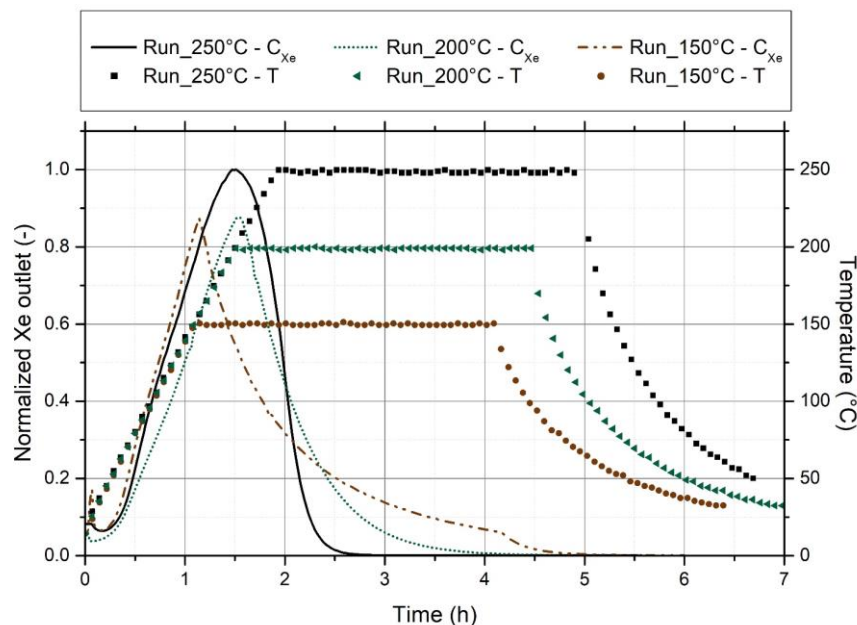


**Figure 10. Normalized Xe desorption curves on the Ag-ETS-10\_2 sample under a helium flow at a temperature of 150 (---), 200 (·····) and 250 °C (—) on the external surface of the adsorption column. The temperature curves for the experiments at 150 (●), 200 (◀) and 250 °C (■) are also presented.**

The choice on the temperature, duration and flow rate will depend on the particular conditions at a facility and can be optimised in function of potential limitations. The use of a higher temperature allows to limit the amount of gas to be used for the desorption and could be an important aspect in the operation of such a system. In addition, a desorption with nitrogen was also investigated at 250 °C (internal temperature of 212 °C) and indicated that the subsequent adsorption with 1000 ppm Xe in He at room temperature remained within the uncertainties of previous adsorption runs. The detailed experimental conditions for these experiments can be found in Supplementary material Table S12. This is highlighted in Table 5 where the Xe adsorption capacity, retention time at 10%, and MTZ percentage during a subsequent adsorption run after a desorption with helium and nitrogen are given. As can be seen in the table, the results obtained during the subsequent adsorption of Xe in He are very similar and within the uncertainties. This indicates that in this heating configuration (temperature, flow rate and duration), helium can be replaced by nitrogen and still provides the same subsequent adsorption efficiency.

**Table 5 – Desorption conditions for the runs with He and N<sub>2</sub> and the results obtained during the subsequent adsorption.**

Desorption				Subsequent adsorption		
Carrier gas	T <sub>set point</sub> (°C)	T <sub>internal</sub> (°C)	t <sub>set point</sub> (h)	q <sub>Xe</sub> (mol/kg)	t <sub>10%</sub> (h)	MTZ (%)
He	250	211	3	0.59	8.4	20%
N <sub>2</sub>	250	212	3	0.61	8.9	15%

### 3.2.7. Durability against desorption/adsorption cycles

Another key aspect of the cost of such a xenon trapping system is the durability of the adsorption material against desorption/adsorption cycles. In total, 20 desorption/adsorption cycles were performed on the same Ag-ETS-10\_2 sample, the detailed experimental conditions can be found in the Supplementary material Table S13. During these cycles, Xe adsorption capacity, retention time at 10%, and MTZ percentage during adsorptions at 1000 ppm Xe in He at room temperature were compared. These parameters are compared in Figure 11 for the relevant cycles. Cycles 9, 10 and 17 corresponded to pulsed experiments and could thus not be compared based on the previous indicators. Also, cycles 18 and 19, corresponding to adsorption experiments at 60 °C, could not be compared based on the previous indicators. Furthermore, cycles 5 and 6, highlighted in red in the figure, corresponded to adsorption runs that occurred after desorption under nitrogen at temperatures about 130 °C, which was clearly not enough to fully desorb xenon with the defined flow rate and duration as can be seen in the figure with the significantly lower adsorption indicators. For the remaining cycles, *i.e.* 1 - 4, 7 - 8, 11 - 16 and 20, called hereafter ‘relevant cycles’, the above mentioned indicators were compared to investigate the durability of the material. It has to be noted that the gamma irradiation mentioned in Section 3.2.4 was done in-between cycle 12 and 13, as indicated by the blue line in Figure 11a. In this figure, the relative deviation for these indicators from the average obtained on the relevant cycles is shown. As can be seen in the figure, Xe adsorption capacity and retention time at 10% are remaining within the 10% uncertainty. Accordingly, no significant effect on Xe adsorption was observed based on these indicators. The average Xe adsorption capacity and retention time at 10% of these relevant cycles was 0.67 mol/g and 9.0 hours respectively for an average Xe partial pressure of 180 Pa and a temperature of 18 °C. On the other hand, as can be seen in Figure 11b, the MTZ percentage is varying much more compared to the two previous indicators, with values ranging from 15% up to 40%. Interestingly, there

are regular steps in the MTZ percentage, occurring between cycle 10 and 11, 12 and 13, 14 and 15, and, 17 and 18, which are corresponding to moments where the adsorbent was removed from the adsorption column, stored for a certain time and then poured back in the column. This is thus likely a consequence of a different packing in the adsorbent test bed and not of a degradation of the material itself as the equilibrium adsorption capacity is still reached.

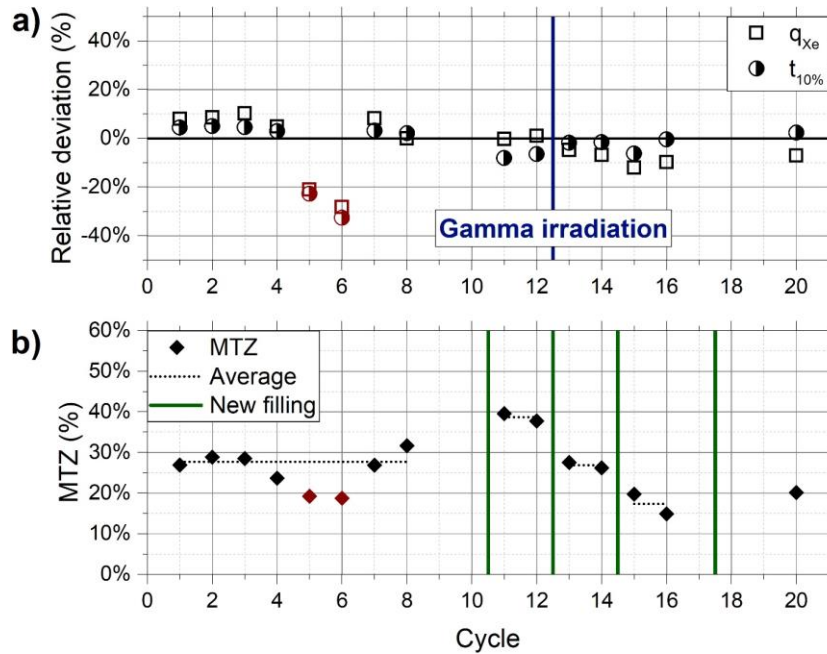


**Figure 11. a) Relative deviation, to the average from the cycles in black, of the Xe adsorption capacity ( $\square$ ) and retention time at 10% ( $\bullet$ ) during the 20 desorption/adsorption cycles on the Ag-ETS-10\_2 sample. The blue vertical line indicates the moment the sample was irradiated. The points indicated in red were obtained after a low temperature desorption. b) MTZ percentage during the 20 desorption/adsorption cycles on the Ag-ETS-10\_2 sample. The green vertical lines indicate the moment the sample was removed from the adsorption test bed and was after a certain time poured back in the test bed. The dotted line corresponds to the average value for each period without consideration of the points indicated in red.**

This is highlighted in Figure 12b, where one breakthrough curve after each filling of the adsorption test bed, *i.e.* cycle 1, 11, 13, 15 and 20, is shown. As could be expected from the MTZ percentages, the shape and slope of the breakthrough curves are very different. This could be explained by a difference in packing after the different fillings, which gave rise to preferential channels for xenon where it encountered less adsorbent material at some locations within the adsorbent bed. This difference in packing was not observed on the measured pressure drop, as the pressure drop along the column, about 100 hPa, was driven by the stainless steel sintered wire mesh and remained at this value for all experiments with the Ag-ETS-10\_2 sample. This could potentially be improved by using a less restrictive wire mesh or a more sensitive pressure drop sensor than the ones used in this work. The uniformity of the packing density could also potentially be improved by using different Ag-ETS-10\_2 particle sizes, which could better fill-in the gaps in the test bed. Shi et al. (2013) demonstrated that by using two different Ag-ETS-10\_2 particle sizes within the same adsorbent bed, a significant increase in packing density could be achieved.

In comparison, breakthrough curves measured during the first filling of the column, except for cycles 5 and 6 for the previously mentioned reasons, are shown in Figure 12a. It is clear from the figure that the shape is very similar for all these breakthrough curves and the differences are within the uncertainties.

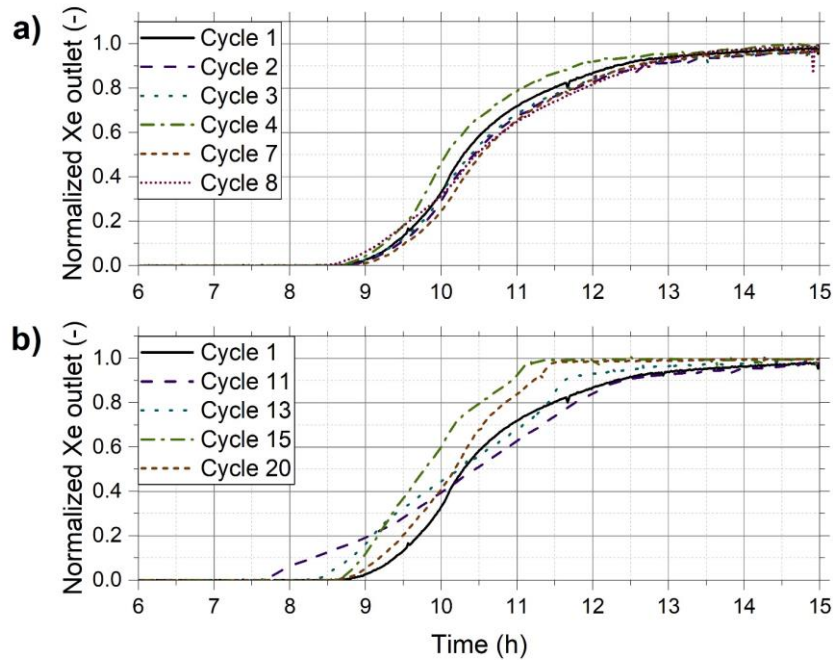


**Figure 12.** a) Normalized Xe breakthrough curves, with 1000 ppm Xe in He at room temperature, on the Ag-ETS-10\_2 sample obtained during the first filling of the adsorption test bed. b) Normalized Xe breakthrough curves, with 1000 ppm Xe in He at room temperature, on the Ag-ETS-10\_2 sample obtained just after a filling of the adsorption test bed.

In view of reducing the operational cost, the reuse of Ag-ETS-10 for successive adsorptions is a key aspect. As it was shown in the previous figures, Ag-ETS-10 can be reused for at least 20 times without significant effect on Xe adsorption properties. According to the obtained results, the packing of the material inside the adsorption column should be carefully executed and controlled in order to eliminate void spaces in between the adsorbent particles, which could cause a faster Xe breakthrough.

#### 4. Conclusions

In this work, Xe adsorption capacities of five silver-exchanged zeolites (AgZs) and three activated carbons (ACs) were compared at room temperature. A silver-exchanged titanosilicate, Ag-ETS-10, showed a much higher Xe adsorption capacity than all other materials, investigated in a range of Xe partial pressures relevant for fission-based medical isotope production facilities. Xe adsorption capacity and Xe retention time at 10% of this AgZ were demonstrated to be a factor 18 to 210 higher than these of a typical nuclear grade AC, depending on the Xe partial pressure and carrier gas. However, a decrease of Xe adsorption capacity was observed at 50% R.H. for this specific AgZ as well as for a Ag-Chabazite sample. Accordingly, the moisture content of the gas stream is a critical aspect for their use for radioxenon mitigation. For all other adsorbents, no significant effect on the Xe adsorption could be observed due to moisture. It was shown that the Xe adsorption kinetics in Ag-ETS-10 could be optimized by adjusting the column geometry and the flow rate of the inlet gas stream. This AgZ was shown to be resistant to a 1 MGy gamma irradiation as well as to 20 desorption/adsorption cycles, allowing the material to be reused for successive Xe adsorptions. Furthermore,

Xe adsorption properties of Ag-ETS-10 were recovered after a desorption at a temperature as low as 150 °C under a helium flow. Such an efficient Xe adsorption material could be used to further decrease radionuclide emissions from these facilities, which in turn would decrease their impact on the IMS network for the CTBT verification.

## Acknowledgements

The financial support from the European Union through the Council Joint Action 2012/699/CFSP of 13 November 2012 and 2018/298/CFSP of 26 February 2018 in support of the Comprehensive Nuclear-Test-Ban Treaty Organization is gratefully acknowledged. The authors would like to thank the two anonymous reviewers for their constructive comments and suggestions.

## References

- Achim, P., Generoso, S., Morin, M., Gross, P., Le Petit, G., Moulin, C., 2016. Characterization of Xe-133 global atmospheric background: implications for the International Monitoring System of the Comprehensive Nuclear-Test-Ban Treaty. *J Geophys Res-Atmos* 121, 4951-4966.
- Achim, P., Generoso, S., Topin, S., Gross, P., Monfort, M., Moulin, C., Le Petit, G., Douysset, G., Morin, M., 2021. 6 months of radionuclide detection in western Europe with the SPALAX-New generation system - Part 2: Atmospheric transport modelling. *J Environ Radioactiv* 226.
- Auer, M., Axelsson, A., Blanchard, X., Bowyer, T.W., Brachet, G., Bulowski, I., Dubasov, Y., Elmgren, K., Fontaine, J.-P., Harms, W., Hayes, J.C., Heimbigner, T.R., McIntyre, J.I., Panisko, M.E., Popov, Y., Ringbom, A., Sartorius, H., Schmid, S., Schulze, J., Schlosser, C., Taffary, T., Weiss, W., Wernsperger, B., 2004. Intercomparison experiments of systems for the measurement of xenon radionuclides in the atmosphere. *Appl Radiat Isotopes* 60, 863-877.
- Banerjee, D., Simon, C.M., Elsaïdi, S.K., Haranczyk, M., Thallapally, P.K., 2018. Xenon Gas Separation and Storage Using Metal-Organic Frameworks (vol 4, pg 466, 2018). *Chem-Us* 4, 650-650.
- Beyer, H.K., Jacobs, P.A., 1982. Chemical Evidence for Charged Clusters in Silver Zeolites, in: Jacobs, P.A., Jaeger, N.I., Jírů, P., Schulz-Ekloff, G. (Eds.), *Studies in Surface Science and Catalysis*. Elsevier, pp. 95-102.
- Bowyer, T.W., 2020. A Review of Global Radionuclide Background Research and Issues. *Pure Appl Geophys*.
- Bowyer, T.W., Eslinger, P.W., Cameron, I.M., Friese, J.I., Hayes, J.C., Metz, L.A., Miley, H.S., 2014. Potential impact of releases from a new Molybdenum-99 production facility on regional measurements of airborne xenon isotopes. *Journal of Environmental Radioactivity* 129, 43-47.
- Bowyer, T.W., Kephart, R., Eslinger, P.W., Friese, J.I., Miley, H.S., Saey, P.R., 2013. Maximum reasonable radionuclide releases from medical isotope production facilities and their effect on monitoring nuclear explosions. *Journal of Environmental Radioactivity* 115, 192-200.
- Braekers, D., Camps, J., Paridaens, J., Saey, P.R.J., Van der Meer, K., 2010. Reduction of radionuclide emissions from radiopharmaceutical facilities - A pilot study, Third European IRPA Congress, Helsinki, Finland.
- Byun, J.I., Hahn, D.S., 2020. Ambient xenon sampling using an Ag/ZSM-5 zeolite. *J Radioanal Nucl Ch* 323, 927-930.
- Carter, J.W., Husain, H., 1974. The simultaneous adsorption of carbon dioxide and water vapour by fixed beds of molecular sieves. *Chem Eng Sci* 29, 267-273.
- Chemviron Carbon, 2005. *Nuclearcarb 203C*.
- Comprehensive Nuclear-Test-Ban Treaty, 1996. Preparatory Commission for the Comprehensive Nuclear-Test-Ban Treaty Organization, Vienna International Center, Vienna, Austria.
- CTBTO, 2021. *CTBTO World Map*.
- Daniel, C., Elbaroui, A., Aguado, S., Springuel-Huet, M.-A., Nossov, A., Fontaine, J.-P., Topin, S., Taffary, T., Deliere, L., Schuurman, Y., Farrusseng, D., 2013. Xenon Capture on Silver-Loaded Zeolites: Characterization of Very Strong Adsorption Sites. *The Journal of Physical Chemistry C* 117, 15122-15129.
- De Meutter, P., Camps, J., Delcloo, A., Deconninck, B., Termonia, P., 2016. On the capability to model the background and its uncertainty of CTBT-relevant radionuclide isotopes in Europe by using ensemble dispersion modeling. *J Environ Radioactiv* 164, 280-290.
- De Meutter, P., Camps, J., Delcloo, A., Termonia, P., 2017. Assessment of the announced North Korean nuclear test using long-range atmospheric transport and dispersion modelling. *Sci Rep-Uk* 7.
- Deliere, L., Coasne, B., Topin, S., Greau, C., Moulin, C., Farrusseng, D., 2016. Breakthrough in Xenon Capture and Purification Using Adsorbent-Supported Silver Nanoparticles. *Chem-Eur J* 22, 9660-9666.
- Deliere, L., Topin, S., Coasne, B., Fontaine, J.P., De Vito, S., Den Auwer, C., Solari, P.L., Daniel, C., Schuurman, Y., Farrusseng, D., 2014. Role of Silver Nanoparticles in Enhanced Xenon Adsorption Using Silver-Loaded Zeolites. *J Phys Chem C* 118, 25032-25040.
- Doll, C.G., Sorensen, C.M., Bowyer, T.W., Friese, J.I., Hayes, J.C., Hoffmann, E., Kephart, R., 2014. Abatement of xenon and iodine emissions from medical isotope production facilities. *J Environ Radioactiv* 130, 33-43.
- Extraordinary Adsorbents, 2021. <https://extraordinaryadsorbents.com/> (Accessed on Nov 28, 2021).
- Faga, P., Moyaux, D., Deconninck, B., 2018. Method for producing a fraction of xenon radioisotopes, in particular Xe-133, fraction of xenon radioisotopes, in particular Xe-133, in: WIPO (Ed.), *WO/2018/002161 Institut National des Radioéléments*.
- Fernandez, A.F., Ooms, H., Brichard, B., Coeck, M., Coenen, S., Berghmans, F., Decreton, M., 2002. SCK center dot CEN gamma irradiation facilities for radiation tolerance assessment. 2002 IEEE Radiation Effects Data Workshop, Workshop Record, 171-176.
- Fujie, K., Nakamura, A., Hidano, T., Kuroda, Y., Mori, T., Torigoe, H., 2010. Xenon Adsorbent, Xenon Enrichment Method, Xenon Enrichment Device, and Air Liquefaction and Separation Device, B01J20/3483 ed.

- Gaebler, P., Ceranna, L., Nooshiri, N., Barth, A., Cesca, S., Frei, M., Grunberg, I., Hartmann, G., Koch, K., Pilger, C., Ross, J.O., Dahm, T., 2019. A multi-technology analysis of the 2017 North Korean nuclear test. *Solid Earth* 10, 59-78.
- Goodwin, M.A., Britton, R., Davies, A.V., 2020. A Consideration of Radioxenon Detections Around the Korean Peninsula. *Pure Appl Geophys.*
- Goodwin, M.A., Davies, A.V., Britton, R., 2021. Analysis of environmental radioxenon detections in the UK. *J Environ Radioact* 234, 106629.
- Gueibe, C., Kalinowski, M.B., Baré, J., Gheddou, A., Krysta, M., Kusmierczyk-Michulec, J., 2017. Setting the baseline for estimated background observations at IMS systems of four radioxenon isotopes in 2014. *J Environ Radioact* 178-179, 297-314.
- Hirano, S., Tokunaga, K., Okaniwa, H., Fukui, M., 2019. Xenon Adsorbent, in: Office, U.S.P.a.T. (Ed.). Tosoh Corporation.
- Hoffman, I., Ungar, R.K., Bean, M., Yi, J., Servranckx, R., Zaganescu, C., Ek, N., Blanchard, X., Le Petit, G., Brachet, G., Achim, P., Taffary, T., 2009. Changes in radioxenon observations in Canada and Europe during medical isotope production facility shut down in 2008. *J Radioanal Nucl Ch* 282, 767-772.
- Ianovski, D., Munakata, K., Kanjo, S., Yokoyama, Y., Koga, A., Yamatsuki, S., Tanaka, K., Fukumatsu, T., Nishikawa, M., Igarashi, Y., 2002. Adsorption of noble gases on H-mordenite. *J Nucl Sci Technol* 39, 1213-1218.
- Kalinowski, M., Axelsson, A., Bean, M., Blanchard, X., Bowyer, T.W., Brachet, G., Hebel, S., McIntyre, J.I., Peters, J., Pistner, C., Raith, M., Ringbom, A., Saey, P.R.J., Schlosser, C., Stocki, T.J., Taffary, T., Ungar, R.K., 2010. Discrimination of Nuclear Explosions against Civilian Sources Based on Atmospheric Xenon Isotopic Activity Ratios. *Pure Appl Geophys* 167, 517-539.
- Kalinowski, M.B., Tatlisu, H., 2020. Global Radioxenon Emission Inventory from Nuclear Power Plants for the Calendar Year 2014. *Pure Appl Geophys.*
- Kepak, F., 1990. Removal of Gaseous Fission-Products by Adsorption. *J Radioanal Nucl Ch Ar* 142, 215-230.
- Kitani, S., Takada, J., 1965. Adsorption of Krypton and Xenon on Various Adsorbents. *J Nucl Sci Technol* 2, 51-56.
- Kuznicki, S.M., Anson, A., Koening, A., Kuznicki, T.M., Hastrup, T., Eyring, E.M., Hunter, D., 2007a. Xenon adsorption on modified ETS-10. *J Phys Chem C* 111, 1560-1562.
- Kuznicki, S.M., Kelly, D.J.A., Bian, J.J., Lin, C.C.H., Liu, Y., Chen, J., Mitlin, D., Xu, Z.H., 2007b. Metal nanodots formed and supported on chabazite and chabazite-like surfaces. *Micropor Mesopor Mat* 103, 309-315.
- Larson, T., Ostman, C., Colmsjo, A., 2011. An automated multidimensional preparative gas chromatographic system for isolation and enrichment of trace amounts of xenon from ambient air. *Anal Bioanal Chem* 400, 449-458.
- Lee, S.K., Beyer, G.J., Lee, J.S., 2016. Development of Industrial-Scale Fission Mo-99 Production Process Using Low Enriched Uranium Target. *Nucl Eng Technol* 48, 613-623.
- Metz, L., Aydia, M., Bigles, C., Bowyer, T.W., Camps, J., Carranza, E., Di Tada, M., Dittrich, S., Friese, J.I., Gueibe, C., Harvey, J., Hoffman, E., Hoffman, I., Ibrahim, H., Ivan, A., Lee, J., Liu, L., Lucas, J., Mahoney, C., McIntyre, J.I., Moyaux, D., Nikkinen, M., Pitas, K., Ridikas, D., Saey, P., Sameh, A.H.A., Sarkis, D., Updegraff, D., Vandegrift, G., 2014. WOSMIP IV - Workshop on Signatures of Medical and Industrial Isotope Production. Report PNNL-23165, Pacific Northwest National Laboratory.
- Moeller, D.W., Underhill, D.W., 1981. Review and Evaluation of Factors Affecting Noble-Gas Adsorption on Activated Carbon. *Nucl Safety* 22, 599-611.
- Monpezat, A., Topin, S., Deliere, L., Farrusseng, D., Coasne, B., 2019. Evaluation Methods of Adsorbents for Air Purification and Gas Separation at Low Concentration: Case Studies on Xenon and Krypton. *Ind Eng Chem Res* 58, 4560-4571.
- Munakata, K., Fukumatsu, T., Yamatsuki, S., Tanaka, K., Nishikawa, M., 1999. Adsorption equilibria of krypton, xenon, nitrogen and their mixtures on molecular sieve 5A and activated charcoal. *J Nucl Sci Technol* 36, 818-829.
- Munakata, K., Kanjo, S., Yamatsuki, S., Koga, A., Ianovski, D., 2003. Adsorption of Noble Gases on Silver-mordenite. *Journal of Nuclear Science and Technology* 40, 695-697.
- Nan, Y., 2017. Adsorption of Iodine and Water on Silver-Exchanged Mordenite, Surface. Syracuse University.
- NEA, 2019. The supply of Medical Radioisotopes: 2019 Medical Isotope Demand and Capacity Projection for the 2019-2024 Period. Nuclear Energy Agency.
- Nucon International Inc., 2002. Nucon Nusorb noble gas delay carbons.
- PNNL, 2018. Workshop on Signatures of Man-Made Isotope Production VI. Report PNNL-26793, Pacific Northwest National Laboratory.
- Puertolas, B., Lopez, M.R., Navarro, M.V., Lopez, J.M., Murillo, R., Garcia, T., Mastral, A.M., 2010. Modelling the Breakthrough Curves Obtained from the Adsorption of Propene onto Microporous Inorganic Solids. *Adsorpt Sci Technol* 28, 761-775.
- Rezaei, F., Webley, P., 2009. Optimum structured adsorbents for gas separation processes. *Chem Eng Sci* 64, 5182-5191.
- Ringbom, A., Axelsson, A., Aldener, M., Auer, M., Bowyer, T.W., Fritioff, T., Hoffman, I., Khrustalev, K., Nikkinen, M., Popov, V., Popov, Y., Ungar, K., Wotawa, G., 2014. Radioxenon detections in the CTBT international monitoring system likely related to the announced nuclear test in North Korea on February 12, 2013. *J Environ Radioact* 128, 47-63.
- Ringbom, A., Axelsson, A., Bjornham, O., Brannstrom, N., Fritioff, T., Grahn, H., Hennigor, S., Olsson, M., 2020. Radioxenon Releases from A Nuclear Power Plant: Stack Data and Atmospheric Measurements. *Pure Appl Geophys.*
- Ruthven, D.M., 1984. Principles of adsorption and adsorption processes.
- Saey, P.R.J., 2009. The influence of radiopharmaceutical isotope production on the global radioxenon background. *J Environ Radioact* 100, 396-406.
- Saey, P.R.J., Bean, M., Becker, A., Coyne, J., d'Amours, R., De Geer, L.E., Hogue, R., Stocki, T.J., Ungar, R.K., Wotawa, G., 2007. A long distance measurement of radioxenon in Yellowknife, Canada, in late October 2006. *Geophys Res Lett* 34.
- Saey, P.R.J., Bowyer, T.W., Ringbom, A., 2010a. Isotopic noble gas signatures released from medical isotope production facilities-Simulations and measurements. *Appl Radiat Isotopes* 68, 1846-1854.
- Saey, P.R.J., Schlosser, C., Achim, P., Auer, M., Axelsson, A., Becker, A., Blanchard, X., Brachet, G., Cella, L., De Geer, L.E., Kalinowski, M.B., Le Petit, G., Peterson, J., Popov, V., Popov, Y., Ringbom, A., Sartorius, H., Taffary, T., Zahringer, M., 2010b. Environmental Radioxenon Levels in Europe: a Comprehensive Overview. *Pure Appl Geophys* 167, 499-515.
- Saey, P.R.J., Wotawa, G., De Geer, L.E., Axelsson, A., Bean, M., d'Amours, R., Elmgren, K., Peterson, J., Ringbom, A., Stocki, T.J., Ungar, R.K., 2006. Radioxenon background at high northern latitudes. *J Geophys Res-Atmos* 111.
- Sameh, A.H.A., 2013. Production Cycle for Large Scale Fission Mo-99 Separation by the Processing of Irradiated LEU Uranium Silicide Fuel Element Targets. *Sci Technol Nucl Ins* 2013.
- Saxton, C.G., Kruth, A., Castro, M., Wright, P.A., Howe, R.F., 2010. Xenon adsorption in synthetic chabazite zeolites. *Micropor Mesopor Mat* 129, 68-73.
- Shi, M., Avila, A.M., Wu, L., Sawada, J.A., Kuznicki, T.M., Kuznicki, S.M., 2013. Air separation by silver titanosilicate with enhanced density. *Sep Purif Technol* 118, 794-800.

- Sokolenko, V.I., Levenets, V.V., Vinokurov, E.I., Grigorova, T.K., Lonin, A.Y., Omelnik, A.P., Sibileva, R.M., Shchur, A.A., 2015. Study of Iodine Adsorption in the Dynamic Mode for Several Carbon Adsorbents. *Probl Atom Sci Tech*, 69-72.
- Underhill, D.W., 1981. Correlation of the Specific Surface-Area and Bulk-Density of Commercial Charcoals with Their Adsorption Capacity for Radioactive Krypton and Xenon. *Nucl Sci Eng* 79, 19-25.
- Underhill, D.W., Dicello, D.C., Scaglia, L.A., Watson, J.A., 1986. Factors Affecting the Adsorption of Xenon on Activated Carbon. *Nucl Sci Eng* 93, 411-414.
- Wotawa, G., Becker, A., Kalinowski, M., Saey, P., Tuma, M., Zahringer, M., 2010. Computation and Analysis of the Global Distribution of the Radioxenon Isotope Xe-133 based on Emissions from Nuclear Power Plants and Radioisotope Production Facilities and its Relevance for the Verification of the Nuclear-Test-Ban Treaty. *Pure Appl Geophys* 167, 541-557.
- Zahringer, M., Becker, A., Nikkinen, M., Saey, P., Wotawa, G., 2009. CTBT radioxenon monitoring for verification: today's challenges. *J Radioanal Nucl Ch* 282, 737-742.
- Zhou, C.Y., Feng, S.J., Zhou, G.Q., Jin, Y.R., Liang, J.F., Xu, J.M., 2011. The behavior of xenon dynamic adsorption on granular activated carbon packed bed adsorber. *J Radioanal Nucl Ch* 287, 609-616.